Received: 7 October 2022 | Accepted: 3 November 2022

DOI: 10.1002/pamm.202200168

Efficient simulation of cables with anisotropic high-order solid finite elements

André Hildebrandt[1,*], **Prateek Sharma**[2], **Stefan Diebels**[2], and **Alexander Düster**[1]

[1] Numerical Structural Analysis with Application in Ship Technology (M-10), Hamburg University of Technology, Am Schwarzenberg-Campus 4 C, D-21073 Hamburg, Germany
[2] Applied Mechanics, Saarland University, Campus A4.2, D-66123 Saarbrücken, Germany

Cables are slender structures with a complex geometry, that can undergo large deformations during their installation or in dynamic environments. In combination with their complex inner structure they pose a challenging problem for finite element simulations. In this article a simplified approach is presented to model cables by using an effective material and a homogeneous cross-section, which is anisotropic in the elastic and inelastic domain. For the high-order hierarchic shape functions with quasi-regional mapping, anisotropic ansatz spaces are applied in tension, torsion and bending simulations. The identification of material parameters is conducted based on experimental results for a tension and a torsion test using the particle swarm optimization algorithm. Finally, the identified parameters are validated for a combined load case with torsion and free bending, showing a promising approach regarding the simulation of cable structures.

1 Introduction

Cables as slender structural members are a common component in engineering structures. They can be used as a structural component in bridges, ski lifts, or tensile structures as well as electrical conductors or to transmit signals. This leads to a large variety of layouts and requirements.

The layout of the cable cross-section often contains several materials like rubbers as insulation and protective jacket, copper or other conductive metals, and sometimes woven fibers, which can serve as an electrical shielding or to improve the structural durability. Considering the different materials, including the interaction between the inner parts based on frictional contact over large areas, leads to numerical challenges and a large computational effort. To decrease the computational cost, the cable is represented by a single material model, that exhibits anisotropies in the hyperelastic and elastoplastic regime [1] and thus does not resolve the inner structure on a geometric level.

In this work we focus on the simulation of a coaxial cable, that exhibits large displacements combined with small or large local strains. These can arise, for example, in a robotic arm or when pulled over edges during their installation. In the finite element framework anisotropic solid elements with high-order hierarchic shape functions [2] are used. Combined with quasi-regional mapping the curved geometry can be accurately represented using only few elements. An anisotropic ansatz can increase the efficiency, while attention has to be paid to the mapping function to prevent the emergence of artificial strains [3]. The effective material properties for the material model are identified with the particle swarm method utilizing experimental tests (tension and torsion) and equivalent FEM simulations. Subsequently, the identified parameters and simulation approach are validated using a bending test combined with torsion.

2 Numerical simulation approach

Due to the large displacements that are exhibited during the simulations the nonlinearity has to be considered in the FEM framework. For this purpose, the most essential parts of the anisotropic material model [1, 4] are presented. First, three principle material directions $\boldsymbol{v}_i$ of the material are introduced which are necessary to define direction dependent invariants of the elastic right Cauchy–Green tensor $\boldsymbol{C}_\mathrm{e}$. These invariants

$$J_i = \mathrm{tr}[\boldsymbol{M}_i \boldsymbol{C}_\mathrm{e}], \quad \text{for } i = 1, 2, 3, \tag{1}$$

$$J_{i+3} = \mathrm{tr}[\boldsymbol{M}_i \boldsymbol{C}_\mathrm{e}^2], \quad \text{for } i = 1, 2, 3, \tag{2}$$

can be computed using a structural tensor $\boldsymbol{M}_i = \boldsymbol{v}_i \otimes \boldsymbol{v}_i$ for $i = 1, 2, 3$, where $\otimes$ denotes the dyadic product. By means of those invariants and the material parameters α_j for $j = 1, ..., 12$, the elastic strain energy density function can be defined,

$$\Psi_\mathrm{e} = \sum_{i=1}^{3} \left[\alpha_i J_i + \frac{\alpha_{i+3}}{2} J_i^2 + \alpha_{i+9} J_{i+3} \right] + \alpha_7 J_1 J_2 + \alpha_8 J_1 J_3 + \alpha_9 J_2 J_3. \tag{3}$$

---

[*] Corresponding author: e-mail andre.hildebrandt@tuhh.de, phone +4940 428 78 2718

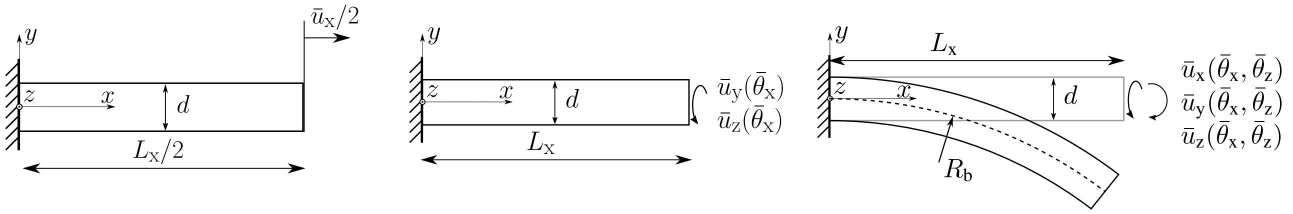

(a) Tension test. **(b)** Torsion test. **(c)** Torsion and free bending test.

Fig. 1: Boundary conditions for the different loading situations.

The material behavior of cables observed in experiments [5, 6] motivates the introduction of an elastoplastic behavior using a multiplicative split of the deformation gradient $\boldsymbol{F} = \boldsymbol{F}_{\mathrm{e}}\boldsymbol{F}_{\mathrm{p}}$.

The orthotropy for the elastoplasticity is incorporated by an orthotropic yield criterion. It is based on six pseudo invariants,

$$I_i = \mathrm{tr}[\boldsymbol{M}_i \mathrm{dev}\boldsymbol{\Xi}], \quad \text{for } i = 1, 2, 3, \tag{4}$$

$$I_{i+3} = \mathrm{tr}[\boldsymbol{M}_i (\mathrm{dev}\boldsymbol{\Xi})^2], \quad \text{for } i = 1, 2, 3, \tag{5}$$

of the stress tensor

$$\boldsymbol{\Xi} = 2\rho_0 \boldsymbol{C}\boldsymbol{F}_{\mathrm{p}}^{-1} \frac{\partial \Psi_{\mathrm{e}}}{\partial \boldsymbol{C}_{\mathrm{e}}} \boldsymbol{F}_{\mathrm{p}}^{-\mathrm{T}}. \tag{6}$$

Again, the invariants depend on the structural tensors $\boldsymbol{M}_i$, which are defined by the material principal directions. The stress invariants can be used together with the material parameters β_j for $j = 1, ..., 9$ to compute an equivalent stress,

$$\chi = \sum_{i=1}^{3} \left[\beta_i I_i^2 + \beta_{i+6} I_{i+3} + \frac{1}{2} \sum_{j=1}^{3} \beta_{i+j+1} I_i I_j \right], \quad \text{for } i \neq j. \tag{7}$$

The material parameters β_j are combinations of the yield stresses σ_{ij}^0 for $i, j = 1, 2, 3$ of the different directions and are discussed in [1, 4]. The equivalent stress together with the nonlinear isotropic hardening

$$Y(Z) = -HZ - (\sigma_\infty - \sigma_{11}^0)(1 - e^{-\eta Z}) \tag{8}$$

is used to define the yield function,

$$\Phi = \sqrt{\frac{2}{3}} \left(\sigma_{11}^0 \sqrt{\chi} - (\sigma_{11}^0 - Y) \right). \tag{9}$$

Here, the variable σ_{11}^0 is the yield stress in direction 1, H is the linear hardening parameter, η is the exponential hardening parameter, and σ_∞ is the saturation stress. These equations are applied together with the principle of maximum dissipation and the Kuhn-Tucker loading/unloading conditions to determine the evolution of the elastoplastic quantities via an exponential map [7] for the time integration. A detailed description of the material model can be found in [1, 3, 4, 6].

2.1 Simulation setup

The simulations resolve the experimental setups only approximately as there are several simplifications and assumptions made for the boundary conditions. These assumptions are shown in Fig. 1, where the sample is clamped on the left-hand side ($u_{\mathrm{x}} = u_{\mathrm{y}} = u_{\mathrm{z}} = 0$), while on the right-hand side displacements are applied according to the different loading cases.

For the tension test in Fig. 1a the symmetry in x-direction at $x = L_{\mathrm{x}}/2$ is exploited to reduce the number of elements used in the simulation. During the torsion test in Fig. 1b the sample can move along the x-axis on the right end, while the displacements in y-direction and z-direction are prescribed according to the applied torsion. For this purpose the position in the reference configuration

$$\boldsymbol{X}(X = L_{\mathrm{x}}, Y, Z) = \boldsymbol{X}(\theta_{\mathrm{x}}, R) = \begin{bmatrix} L_{\mathrm{x}} \\ R\cos(\theta_{\mathrm{x}}) \\ R\sin(\theta_{\mathrm{x}}) \end{bmatrix}, \tag{10}$$

$$R = \sqrt{Y^2 + Z^2}, \tag{11}$$

$$\theta_{\mathrm{x}} = \cos^{-1}\left(\frac{Y}{R}\right), \quad \text{if } Z < 0, \ \theta_{\mathrm{x}} = \theta_{\mathrm{x}} + \pi, \tag{12}$$

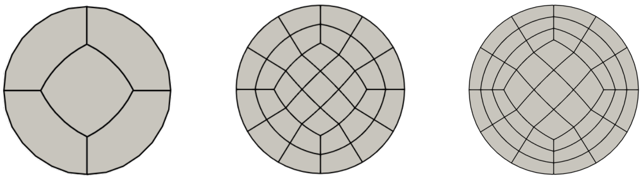

(a) Cross-section M_1. **(b)** Cross section M_2. **(c)** Cross section M_3.

Fig. 2: Mesh layout.

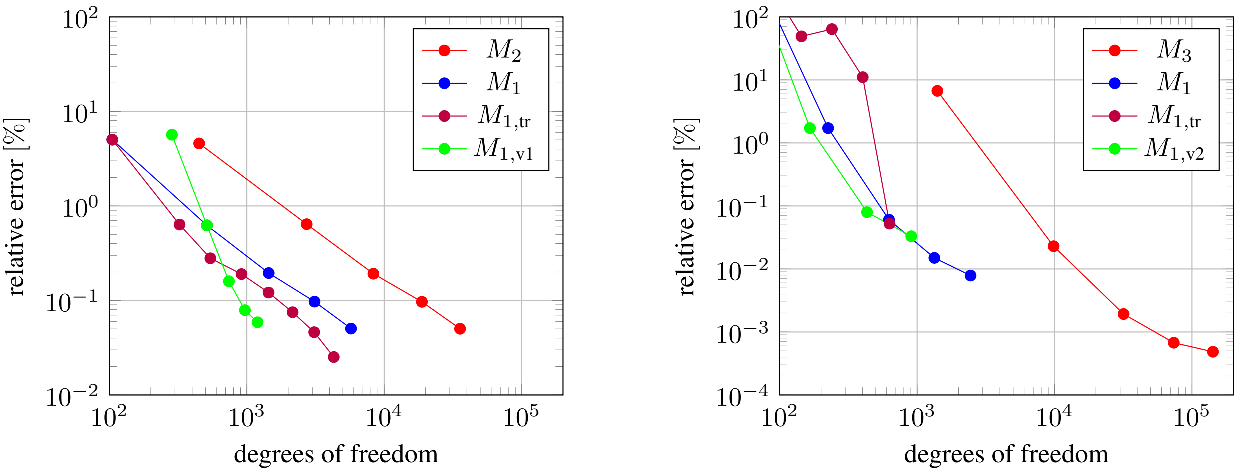

(a) Tension. **(b)** Torsion.

Fig. 3: Comparison of ansatz spaces during p-refinement for tension and torsion [6].

is described in terms of polar coordinates θ_x and R. Using the polar coordinate description a torsion $\bar{\theta}_\text{x}$ can be prescribed and the resulting displacements are computed by

$$\bar{\boldsymbol{u}}_\text{tor} = \boldsymbol{X}(\theta_\text{x} + \bar{\theta}_\text{x}, R) - \boldsymbol{X}(\theta_\text{x}, R) = [\bar{u}_\text{x,tor}, \bar{u}_\text{y,tor}, \bar{u}_\text{z,tor}]^\text{T}. \tag{13}$$

Please note that the displacements in x-direction $\bar{u}_\text{x,tor}$ are not prescribed, as indicated in Fig. 1b. The original length L_x of the cable can change due to the torsion deformation, which has to be considered during the combination of free bending with torsion. Thus, the length used for the computation of the prescribed bending deformation is updated after applying the torsion and is labeled $\tilde{L}_\text{x}$. During free bending or the combination of torsion and free bending the displacements are calculated based on the assumption, that a circular arc with radius

$$R_\text{b} = \frac{\tilde{L}_\text{x}}{\bar{\theta}_\text{z}}, \tag{14}$$

is formed by the sample. It is only used, if bending is prescribed ($\bar{\theta}_\text{z} > 0$) to prevent an infinitely large radius. The bending deformation

$$\bar{\boldsymbol{u}}_\text{bend} = \begin{bmatrix} R_\text{b}\sin(\bar{\theta}_\text{z}) - \tilde{L}_\text{x} \\ R_\text{b}(\cos(\bar{\theta}_\text{z}) - 1) \\ 0 \end{bmatrix} + \begin{bmatrix} (Y + \bar{u}_\text{y,tor})\sin(\bar{\theta}_\text{z}) \\ (Y + \bar{u}_\text{y,tor})(\cos(\bar{\theta}_\text{z}) - 1) \\ \bar{u}_\text{z,tor} \end{bmatrix}, \tag{15}$$

is a superposition of the translation of the neutral axis, represented by the first part in eq. (15) and the rotation of the surface itself (torsion rotation + bending rotation) in the second part of eq. (15).

To ensure an efficient computation, especially during the parameter identification, a convergence study for the tension and torsion test is presented in Fig. 3. In Fig. 3(a) a comparison for the simulation of the tension test using p-refinement and four different meshes is illustrated. The mesh refinement can be seen in Fig. 2, where both M_1 and M_2 use four elements in axial direction. The comparison of M_1 and M_2 shows clearly, that a further h-refinement improves the solution only marginally, while the p-refinement leads to a faster convergence. The convergence can be improved utilizing the trunk ansatz space ($M_{1,\text{tr}}$) [2] and shows, that with less than 1000 degrees of freedom the three-dimensional model is already in an error margin of less than 1%.

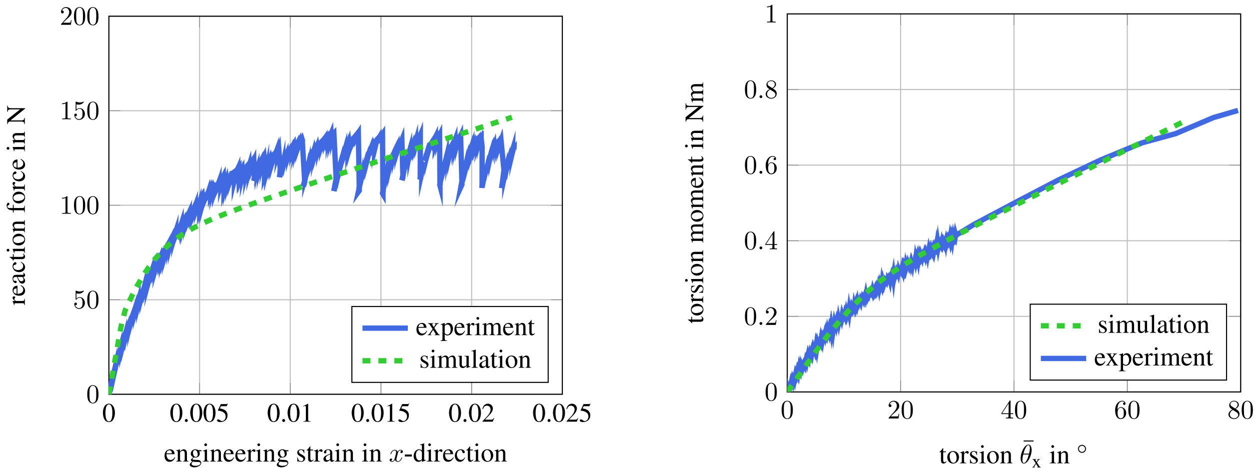

(a) Tension.

(b) Torsion.

Fig. 4: Comparison of experimental curves and parameter identification simulations [6].

A look at the convergence for the torsion simulations in Fig. 3(b) reveals that the h-refinement ($M_1 \rightarrow M_3$) shows a larger increase in accuracy compared to the tension test. M_1 and M_3 use eight elements in axial direction, as there is no symmetry applied along the x-axis . The p-refinement again shows an improved convergence with respect to the degrees of freedom. In contrast to the tension test, the trunk space offers only an improvement for higher order ansatz functions from $p \geq 5$. This is an effect based on the reduced number of face modes, which is further elaborated in [2, 3]. Still, less than 1000 degrees of freedom are necessary to represent the torsional moment with an accuracy below 1%.

Choosing the ansatz order template to be anisotropic

$$\boldsymbol{p}_{\mathrm{v}1} = \begin{bmatrix} p_1 & p_1 & p_1 \\ 2 & 2 & 2 \\ 2 & 2 & 2 \end{bmatrix}, \qquad \boldsymbol{p}_{\mathrm{v}2} = \begin{bmatrix} 1 & p_1 & p_1 \\ 1 & p_1 & p_1 \\ 1 & p_1 & p_1 \end{bmatrix}, \tag{16}$$

leads to the convergence curves in green, where the template $\boldsymbol{p}_{\mathrm{v}1}$ is used in the tension test and $\boldsymbol{p}_{\mathrm{v}2}$ in the torsion test. During the tension test, the orders of the local element direction aligned with the x-axis are increased, while the remaining orders are fixed at $p = 2$. The geometric description of the elements is based on the quasi-regional mapping, that applies an order of two. In the torsion test the orders of all three local element directions describing the displacements in x-direction are kept constant at $p = 1$, while the remaining ansatz orders are increased. The anisotropic convergence curves show a slight improvement depending on the accuracy requested. A more detailed explanation of the anisotropic ansatz space and its implications with regards to the quasi-regional mapping is discussed in [3].

2.2 Parameter identification

The parameter identification is conducted using the particle swarm method of the MATLAB optimization toolbox to optimize the material parameters towards a set, able to represent the experimental results.

In a first step, the material model using orthotropy is reduced to transverse isotropy, since coaxial cables exhibit approximately rotational symmetry in their structural composition. This implies for the Young's moduli $E_2 = E_3$, the shear moduli $G_{12} = G_{13}$, $G_{23} = \frac{E_2}{2(\nu_{23}+1)}$, and the Poisson's ratios $\nu_{12} = \nu_{13}$ of the elastic material parameters. In the elastoplastic domain only the yield stresses are affected: $\sigma_{22}^0 = \sigma_{33}^0$, $\sigma_{12}^0 = \sigma_{13}^0$, and $\sigma_{23}^0 = \sqrt[3]{\sigma_{22}^0}$ for the inelastic material parameters.

In a second step, an insensitivity of the parameters ν_{12}, ν_{23}, and σ_{22}^0 with respect to the measured reactions has been found, which motivates further the assumptions of $\nu_{12} = \nu_{23} = 0.3$ and $\sigma_{11}^0 = \sigma 22^0$. This leaves a total number of 8 independent material parameters to be identified.

3 Experimental and numerical results

The identification results of the material parameters for the coaxial cable are presented in Fig. 4. The simulations are depicted in green and represent the best fit that was achieved with the particle swarm method. The tension test in Fig. 4a shows that the experiments have large noise and a constant increase-decrease pattern in the elastoplastic domain. This is likely due to a stick-slip behavior between the inner parts of the cable.

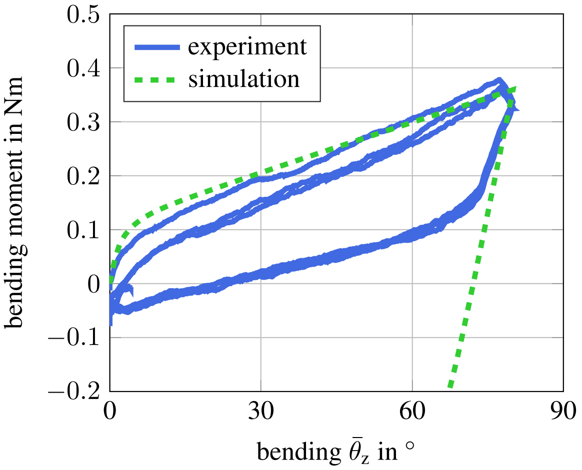

Fig. 5: Experimental and simulation results for free bending [6].

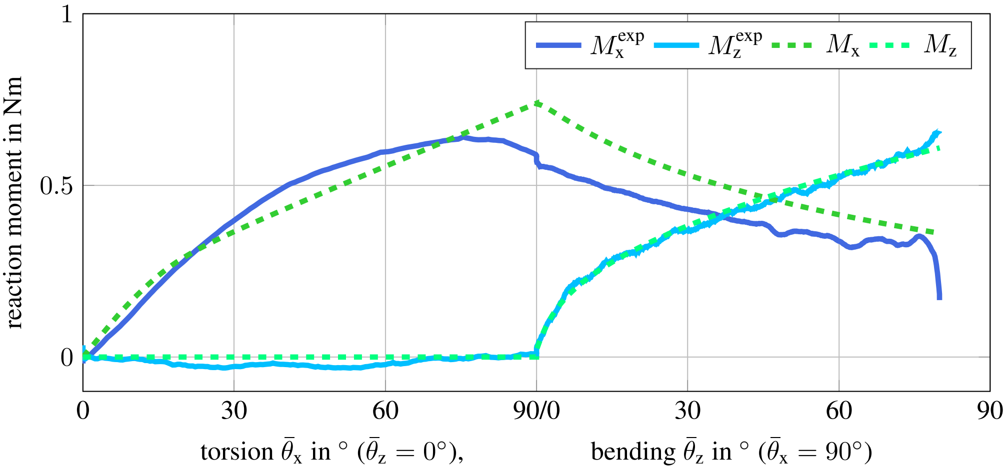

Fig. 6: Experimental and simulation results for torsion and bending loading [6].

The simulation presents an acceptable fit for the elastic part in the beginning, while exhibiting a large discrepancy in the elastoplastic regime. After an engineering strain of approximately 0.005 the elastoplastic hardening turns linear, which indicates a saturation of the nonlinear isotropic hardening, such that the linear hardening dominates the behavior.

The torsion simulation in Fig. 4b is a good fit to the experimental curve for the identified material parameters. It reflects the elastic behavior in the beginning and the inelastic behavior starting around 10° of torsion satisfactorily.

A validation of the identified material parameters is done by a free bending test, that is shown in Fig. 5. The elastic loading is only present for a very small bending angle between ca. 0° and 2°, where-after the nonlinear hardening is visible, that quickly turns to linear hardening after about 5° bending. Both, the elastic and elastoplastic regime fit well with the simulation results. The unloading can be predicted by the simulation for ca. 80° to 70° well. At further unloading the simulation stays elastic, which is expected for material models using isotropic hardening. The experimental curve in contrast reduces its slope. The change in the slope reminds of the translation of the yield surface described by kinematic hardening and can possibly be described by this. But in the unloading between 80° and 70° the expansion of the yield surface described by the isotropic hardening is also visible, as the elastic region has increased.

In Fig. 6 the combination of torsion in the first half and free bending in the second half is depicted. In dark blue (experiment) and dark green (simulation), the torsional moment (M_x) is visible and both curves have a close resemblance. At about 80° torsion the experiment shows a softening, that is not reproduced by the simulation. This softening was not observed in the torsion experiment in Fig. 4b used for the parameter identification. Thus it is not surprising, that it is not present in the torsional loading during the coupled simulation. This leads to an offset that only slowly shrinks during the bending deformation, while showing qualitatively the same behavior. The bending moment (M_z) is shown in light blue (experiment) and light green (simulation). Both curves fit very well during the whole deformation process.

Comparing the bending moment during the free bending in Fig. 5 and the bending moment during free bending with pre-torsion in Fig. 6, the observed curves change. The pre-torsion increases the elastic region of the loading curve and thus allows for a higher overall bending moment, while the qualitative behavior stays the same. This quantitative change in behavior is also reflected by the simulation and shows that the model is able to represent the coupling between torsion and bending of the cable.

4 Conclusion

The usage of high-order shape functions combined with quasi-regional mapping offers advantages in accuracy with respect to the degrees of freedom of the overall system. To further improve those aspects, the trunk space or anisotropic ansatz spaces can be employed.

The comparison of experimental results and simulations shows, that the high-order FEM framework in combination with the chosen material model can be used to efficiently compute the mechanical behavior of the cables. This is evident from the good representation of the bending moment in the free bending test and the coupled loading of torsion and bending, where the changed behavior can be captured by the simulation. Nevertheless, there are some discrepancies as the model is not able to reproduce the measured softening of the torsion moment in the combined loading. The stick-slip effect in the tension test is a result of the clamping in the physical experiment and thus can be either addressed by changing the experimental set-up or by changing the simulation. Within the simulations the boundary conditions play a crucial role, as they represent many assumptions made during the abstraction of the experiments. Furthermore, improvements for the unloading are possible, which can potentially be achieved by including kinematic hardening. Alternatively the cable can be resolved more accurately with respect to the mesh. This can be done by meshing the single layers of the coaxial cable and attributing them individual material properties, resulting in a more complex and flexible overall behavior.

Acknowledgements The support of the DFG (Deutsche Forschungsgemeinschaft) under grant number DU 405/14-1 and DI 430/43-1 is gratefully acknowledged. Open access funding enabled and organized by Projekt DEAL.

References

[1] C. Sansour, I. Karšaj, and J. Sorić, Int. J. Plast. **22**(12), 2346-2365 (2006).
[2] A. Düster, H. Bröker, and E. Rank, Int. J. Numer. Methods. Eng. **52**(7), 673-703 (2001).
[3] A. Hildebrandt and A. Düster, Int. J. Comput. Methods **19**(5), 2250007 (2022).
[4] C. Sansour, I. Karšaj, and J. Sorić, J. Comput. Phys. **227**(16), 7643-7663 (2008).
[5] V. Dörlich, J. Linn, and S. Diebels, Arch. Mech. Eng., **63**(2), 215-230 (2016).
[6] A. Hildebrandt, S. Prateek, A. Düster, and S. Diebels, Math. Mech. Solids **27**(10), 2314-2337 (2022).
[7] A. Eterovic, and K Bathe, Int. J. Numer. Methods. Eng. **30**, 1099-1114 (1990).